Geocarto International, Volume 37, Issue 22, 2022, pp. 6579-6601
DOI:10.1080/10106049.2021.1953617

An integrated ASTER-based approach for mapping carbonatite and iron oxide-apatite deposits

Cheikh-Elwali Malainine [a,b,*], Otmane Raji[a], Muhammad Ouabid[a], Abdou Khouakhi [c], Jean-Louis Bodinier [a,d], Ahmed Laamrani[e], Hicham El Messbahi[f], Nasrrddine Youbi [b,g], and Moulay Ahmed Boumehdi[b]

[a]Mohammed VI Polytechnic University (UM6P), Geology & Sustainable Mining, Benguerir, Morocco

[b]Cadi Ayyad University, Faculty of Sciences-Semlalia, Department of Geology, Marrakech, Morocco

[c]School of Water, Energy and Environment, Centre for Environmental and Agricultural Informatics, Cranfield University, UK

[d]University of Montpellier, Montpellier, France

[e]Center for Remote Sensing Applications (CRSA), UM6P, Benguerir, Morocco

[f]Department of Geology, Sidi Mohamed Ben Abdallah University, Taza, Morocco

[g]Faculty of Geology and Geography, Tomsk State University, Tomsk, Russia

[*]cheikh-elwali.malainine@um6p.ma

Abstract

Mapping of carbonatites and related mineral deposits has occupied prominent place in mineral resource exploration programs given their potential to host valuable concentrations of critical metals such as rare earth elements and niobium. Based on spectral characteristics of most indicative minerals for these rocks, a mapping approach was developed using Advanced Spaceborne Thermal Emission and Reflection Radiometer (ASTER) data. The combination of band rationing outcomes with components from the principal component analysis and minimum noise fraction techniques highlighted the targeted rocks, with the excellent prospective zone representing ~ 0.2% of the total investigated area. This approach was successfully applied to the Gleibat Lafhouda complex to rapidly delineate carbonatites and iron oxide-apatite ore outcrops. Results were validated through field observations and in-situ geochemical analysis using a portable X-ray fluorescence analyzer. Field data have also served as training data to perform a supervised classification, allowing further improvement of the mapping results.

Keywords Remote sensing, ASTER data, mineral resource exploration, carbonatite, iron oxide-apatite ore

1. Introduction

Carbonatites and alkaline-carbonatite complexes are the primary sources for several strategic metals such as rare earth elements (REE) and niobium (Nb), which are vital in the development of emerging industries and green technologies (e.g., Mariano 1989; Chakhmouradian et al. 2015; Verplanck et al. 2016; Wang et al. 2020). They also host considerable apatite deposits that are often related to magmatic and/or weathering processes (e.g., Willet et al. 1989; Toledo et al. 2004; Zaitsev et al. 2015; Ouabid et al. 2021). Some of these deposits have been mined to produce critical metals

and fertilizer in different parts of the world such as in Siilinjärvi, Finland, (O'Brien et al. 2015); Khibina in Kola Peninsula, Russia (Zaitsev et al. 2015; Kogarko 2018); Phalaborwa, South Africa (Vielreicher et al. 2000); Catalão, Brazil (Oliveira and Imbernon 1998). Consequently, many exploration programs worldwide have been launched in the last decades for carbonatite and associated deposits to develop and diversify the supply source for critical metals. The occurrences of carbonatites outcrops in largely remote areas, makes the adoption of remote sensing data to map, delineate, and discover these complexes a time- and cost-effective approach, especially in vast and arid regions.

The Advanced Spaceborne Thermal Emission and Reflection Radiometer (ASTER) data have been successfully used for mapping and investigating carbonatite complexes in many areas by using a variety of processing techniques. One of the relevant studies has used the ASTER Thermal Infrared (TIR) band rationing (B13/B14) and decorrelation stretch (bands: 13, 12, and 10 displayed in RGB, respectively) to highlight the carbonatite outcrops of the Khanneshin volcano in Afghanistan; and matched filtering for mapping the distribution of calcitic and ankeritic carbonatites (Mars and Rowan 2011). Another study by Rajendran and Nasir (2013a) has used the spectral absorption properties to distinguish carbonatite in greyscale and RGB images by white pixels in the TIR region and dark pixels in the Visible and Near Infrared-Short Wave Infrared (VNIR-SWIR) region owing to the molecular emission and absorption characters of carbonate minerals. These authors have also used the ASTER VNIR-SWIR data through Principal Component Analysis (PCA) technique to highlight carbonatite outcrops in Batain Nappe of Oman. However, the presence of lithological facies with similar spectral characteristics in the same area has probably complicated their task based only on one method such as grey image visualization, band ratio, or color composite. Indeed, the ASTER spectral features of carbonates such as absorption in band 8 could be confused with the absorption of ferromagnesian minerals (e.g., olivine, amphibole, serpentine) which due to Mg-OH absorption near 2.3 µm in band 8 (e.g., Baldridge et al. 2009).

Morocco hosts several carbonatite and carbonatite-alkaline complexes that are associated with potential resources of critical metals such as: (1) Tamazight complex in the High Atlas belt (Bouabdli et al. 1988; Marks et al. 2008; Bouabdellah et al. 2010), (2) the Cretaceous Twihinate and (3) the Paleoproterozoic Gleibat Lafhouda carbonatites in the western and eastern parts of the Oulad Dlim massif, respectively (e.g., Qalbi et al. 2011; Montero et al. 2016). Preliminary investigations conducted by the Moroccan national office of hydrocarbon and mines (ONHYM) in the Gleibat Lafhouda carbonatite complex have revealed promising REE and Nb resources mostly linked to associated iron oxide-apatite (IOA) mineralization: up to ~100 Mt with 0.2 wt.% REE and 0.3 wt.% Nb_2O_5 (ONHYM 2016a, b). Despite these potential mineral resources, the geology of the Oulad Dlim massif remains poorly understood because of accessibility issues. The 1:1,000,000 Geological Map of Morocco (Bronner et al. 1985) is the only available complete geological map of the massif with few higher resolution geological maps (1:50,000; https://cartesgeoscientifiques.mem.gov.ma/catalogue). Therefore, a new geological mapping approaches based on the interpretation of satellite imagery can contribute in improving our understanding of this area's geology. The present study highlights the potential of processing data recorded by ASTER sensor to identify and map carbonatite complexes and related mineral deposits. In this context, the enhancement of ASTER imagery by the combination of several image processing techniques [band rationing, PCA, minimum noise fraction (MNF), and supervised classification (SC)] is used here to highlight the extension of carbonatite bodies and associated iron oxide-apatite ores. The integration of these multitechniques was to avoid false anomalies and enhance accuracy mapping accuracy. This approach has been applied in the Gleibat Lafhouda carbonatite complex, south of Morocco (Fig. 1) in order to assess its efficiency, using field and petrographic observations, and in-situ geochemical X-ray fluorescence analysis for validation (e.g., Raji et al. 2021 and references therein).

2. Geological setting of the study area

This study was conducted in the Oulad Dlim massif, which is a vast zone of desertic terrains (~ 36,000 km^2) located in the west margin of the Reguibat Shield (Fig. 1). The westernmost part of the Reguibat shield straddling southern Morocco is recognized as the Awserd-Tichla area according to the nomenclature of Rjimati and Zemmouri (2002). It consists of the Aghaylas suite (2.9 − 3.0 Ga; Montero et al. 2014)**,** and is formed essentially by tonalites and trondhjemites with minor granodiorites and granites locally migmatised. This northwestern part of the West African Craton is marked by the Oulad Dlim massif, also known as the Adrar Souttouf massif (e.g., Bronner et al. 1985; Gärtner et al. 2016). It consists of geotectonic units superimposed above each other with eastward vergence, and forms with the Mauritanides s.s. the western peri-cratonic envelope of the Reguibat Shield (e.g.,Villeneuve et al. 2006; Michard et al. 2008; Villeneuve et al. 2010; Michard et al. 2010; Rjimati et al. 2011). These geotectonic units overlie the Archean basement either directly or through a thin band of Paleozoic sediments of the Dhloat Ensour Group (e.g., Sougy 1962; Rjimati and Zemmouri 2002; Gärtner et al. 2017). The Gleibat Lafhouda carbonatites intrude the orthogneisses and paragneisses which alternate locally with metasediments of the most eastern Archean unit of the Oulad Dlim massif (ca. 2.94–3.12 Ga; Bea et al. 2016, 2020). Three mains separated magnesiocarbonatite intrusions shaped the form of the Gleibat Lafhouda complex: Gleibat Lafhouda s.s., and Gleibat Drag which are the largest ones, and Gleibat Al Fernan in the northeastern part (Fig. 1). The carbonatite intrusions are well exposed in the Saharan desert and cover an area of ~ 150 km^2. Most of these carbonatite bodies are associated with the dark to brown apatite-rich iron oxide mineralization, which overlies the carbonatite with a direct contact (e.g., Benaouda et al. 2020). The eastern unit of the Oulad Dlim massif is limited to the west by Ediacaran metamafic rocks of the Adrar Souttouf massif s.s. They are formed by the accumulation of amphibolites (ca. 603 ± 1.5 Ma) and granulites (ca. 605 − 420 Ma) of gabbroic composition and alternate locally with some granitic gneisses and metasedimentary rocks (e.g., Bea et al. 2020).

3. Data and methods

3.1. Data acquisition and pre-processing

We used two multispectral ASTER level 1 T scenes (AST_L1T) covering the Gleibat Lafhouda region (Table 1). The data are downloaded from the Land Processes Distributed Active Archive Center (LP DAAC;https://LPDAAC.usgs.gov). The AST_L1T radiance data are produced from AST_L1B, which have been geometrically corrected, and projected into Universal Transverse Mercator (UTM)_zone 28 North (Duda et al. 2015). ASTER is a multispectral sensor launched in 1999 onboard the Earth Observing System (EOS) Terra platform. The usefulness of ASTER data has been proved for mineral exploration and geological mapping by several studies (e.g., Mars and Rowan 2011; Rajendran and Nasir 2013b; Ninomiya and Fu 2016; Yazdi et al. 2018; Abdelkareem and El-Baz 2018; Shi et al. 2020; Khan et al. 2020; Beirami and Tangestani 2020). ASTER sensor has relatively ameliorated spatial, spectral, and temporal resolutions compared to most other multispectral sensors such as Landsat. It measures reflected radiation in nine bands between 0.52 to 2.43 μm (VNIR-SWIR) with 15 to 30 m resolution (Fujisada 1995; Abrams 2000). Additionally, ASTER has five bands in the thermal infrared wavelength region between 8.125–11.65 μm with 90 m resolution (Table 2). This makes ASTER sensor more suitable for discrimination and mapping of carbonatites and related deposits.

The ASTER TIR data were used with band rationing, without any atmospheric correction to avoid the influence of correction algorithms on the originated spectral data (e.g., Ninomiya et al. 2005). On the other hand, the VNIR and SWIR bands were co-registered in one file of nine bands and resampled to 15 m spatial resolution. Then, they were atmospherically corrected using the FLAASH (Fast Line of sight Atmospherics Analysis to Hypercubes) module (e.g., Cooley et al.

2002) for converting radiance data to surface reflectance and eliminating the effects caused by water vapor and cloud cover. Finally, several algorithms of image enhancements were applied on the VNIR and SWIR data such as PCA, MNF, and band rationing. The workflow chart summarizing the methodology adopted in this paper is shown in Figure 2.

3.2. Band ratio TIR and VNIR-SWIR

Band rationing is a widely used approach for identifying and mapping various mineral concentrations, hydrothermal alteration/weathering profiles and rock types (e.g., Ninomiya et al. 2005; Pour and Hashim 2011; Mars and Rowan 2011; Guha and K 2016; Ninomiya and Fu 2016; Fakhari et al. 2019; Zamyad et al. 2019; Khan et al. 2020). It is the ratio of the digital number (DN) of each pixel in a given band and the DN of the equivalent pixel in another band, which highlights the desired object in bright pixels. The choice of the appropriate band ratio is based particularly on the spectral absorption and reflection features of the material and its abundance in the scene (Clark 1999; Sabins 1999). The carbonate minerals (calcite and dolomite) as major components of carbonatites in our case, have several diagnostic spectral signatures. They can be distinguishable in the thermal infrared spectroscopy between 11.35 and 11.40 μm, and in the VNIR-SWIR region between 2.33 and 2.45 μm due to the spectral absorption of CO_3^{-2} anions in the electromagnetic spectrum (e.g., Hunt 1977; Clark 1999; Ninomiya 2002; Mars and Rowan 2010; Rajendran and Nasir 2014). The Fe-oxide/hydroxides have spectral features around 0.45 μm and 0.85 μm related to the ferrous (Fe^{2+}) and ferric (Fe^{3+}) iron absorptions in the VNIR region (Clark 1999). These characteristics in respect to ASTER's spectral bands were used to choose the most appropriate band ratio in both TIR and VNIR-SWIR regions for detecting carbonatites and associated iron oxide-apatite mineralization. Therefore, the spectral curves of the major mineral phases encountered in carbonatites and IOA ore were resampled to ASTER bandpass from the USGS spectral library (Kokaly et al. 2017).

In order to assess the performance of the used band ratios, we established a database of previously known carbonatites and IOA mineralization occurrences (Montero et al. 2016; Benaouda et al. 2020). Then the digital numbers of each band ratio and the corresponding sample from the database were plotted in the Receiver Operating Characteristic (ROC) curves (Nykänen et al. 2015). The curve was performed by plotting sensitivity (also known as true positive rate) against 1-specificity (false positive rate) at varying thresholds. The Area Under Curve (AUC) was used as an indicator to quantify the performance of the various band ratios used.

3.3. Dimensionality reduction techniques

The PCA and the MNF are well-known techniques of multivariate statistics that convert a set of initially correlated variables into independent or uncorrelated components. PCA is a robust technique that can be used for enhancing spectral reflectance features for geological application by suppressing irradiance effects (e.g., Tobin 2007). Besides, the MNF as PCA is known to be an efficient technique for reducing initially a large data set to a smaller number of components that contain low incoherent data and most inherent spectral information (Green et al. 1988). These two methods were compared and integrated with band ratios to better highlight carbonatite outcrops and associated IOA mineralization. In order to avoid a particular spectral contrast and increase the chance to define a distinctive component for the desired material, these techniques were applied on a specific subset of ASTER spectral data (Loughlin 1991; Crósta et al. 2003). The selected spectral bands were chosen following the absorption and reflection diagnostic features of the target minerals in the VNIR and SWIR ranges. The choice of the appropriate component in each method was based on analyzing the resulted eigenvector matrix.

The anomalous pixels in each method were combined by reclassifying the results in Geographic Information System (Arc GIS 10.8). The pixels that highlight the desired material were assigned 1 while the other pixels were given 0. Then an integrated map with different classes was generated. The obtained classes were visualized to analyze the number of methods involved in the anomalous areas.

3.4. Field validation and X-ray analysis

The fieldwork was carried out in the Gleibat Lafhouda area to evaluate the resulted maps and to investigate the occurrence and distribution of carbonatite rocks and associated IOA mineralization. In-situ geochemical analyses of about 80 samples were performed. For this purpose, the Handheld X-ray florescence (XRF) Niton XL5 analyzer was used as it represents a powerful tool for rapid collection of large compositional data sets which are important for geostatistical purposes (Young et al. 2016). This technique gives generally comparable results with laboratory analysis for most elements with the advantage of providing fast and real-time geochemical information. Two international reference standards (CG-2, OPY-1) were analyzed to assess the precision of the acquired data, and they have shown good agreement with the proposed values from GeoReM database (http://georem.mpch-mainz.gwdg.de). Based on field observations and the collected geochemical database, several samples representing the encountered facies were selected for further petrographic analysis using standard microscope Leica DM2700P.

3.5. Supervised classification

The obtained results were used as training classes to perform a supervised classification using the Maximum Likelihood (ML) algorithm. The ML classifier is one of the most used methods for satellite image classifications (e.g., Xiuping Jia and Richards 1994; Ahmad and Quegan 2012). It is based on a discriminant function that assigns each pixel to the appropriate class with the highest likelihood. The accuracy of the ML classification was assessed using a confusion matrix, which is based on the comparison of the reference data and the corresponding results.

4. Results

4.1. Mapping of carbonatites

The spectral signatures of calcite and dolomite (Fig. 3) show the maximum absorption in band 14 with high emissivity in band 13. The dolomite exhibits a high emissivity decrease than calcite between band 13 and band 14, which gives the dolomitic rocks the susceptibility to have high carbonates index values than limestone and other calcite-rich rocks. Therefore, the ratio of band 13 and band 14 was used here to highlight the magnesiocarbonatite (i.e., dolomite-rich carbonatites) outcrops over our region of interest. The observed maximum absorption in band 8 for calcite and bands 7 and 8 for dolomite, has given the following band ratios as the most optimum options: (B6/B8)*(B9/B8), (B6+B8)/B7, (B6+B9)/B7 and (B6/B7)*(B9/B8)

Among the computed band ratios, B13/B14 has the highest AUC value (0.83) compared to the other band ratios in the SWIR region (Fig. 4). Additionally, the ratio B6+B9/B7 showed a good performance with AUC= 0.72 compared to the other band ratios showing AUC ranging from 0.66 to 0.71. Therefore, only these two band ratios B13/B14 and B6+B9/B7 have been considered to map the carbonatite outcrops over the Gleibat Lafhouda area. Figure 5 shows the targeted carbonate-rich lithologies highlighted in bright pixels.

As observed in Figure 3, the most indicative minerals for carbonatite (i.e., calcite, dolomite, hematite, apatite, and phlogopite) show variation in absorption between bands 1–2 in the VNIR and between bands 5–8 in the SWIR. Hence, bands 1, 2, 5, and 8 were selected as the input to the PCA and MNF methods for mapping carbonatite rocks. The PCA eigenvectors obtained from the processed ASTER bands (1, 2, 5, and 8) show the different contributions of each band in the resulted component (Table 3). The PC4 displays negative eigenvector loading, with opposite signs in bands 1, 2 (0.713, −0.547, respectively) and bands 5, 8 (-0.283, 0.336, respectively). This relevant difference is consistent with the observed spectral behavior of the indicative minerals in carbonatite such as calcite, dolomite, apatite, and phlogopite (Fig. 3). Since the eigenvectors present a reverse trend compared to the spectral profiles of target minerals, the expected carbonatite areas appear in this component as dark pixels (Fig. 6a). Thus, the PC4 was chosen among the other component to enhance the outcropped carbonatite areas.

The selected spectral subset of ASTER data used as input in the MNF method is the same as that used for PCA (i.e., bands 1, 2, 5 and 8). The resulted transformation vectors are shown in Table 4. The MNF4 shows a highly positive contribution of bands 5 (0.803) with opposite (negative) contributions of bands 1, 2, and 8 (-0.400, −0.283, and −0.338 respectively). This trend is relatively identical to the most prospective minerals of carbonatite (e.g., calcite, dolomite, apatite, and phlogopite), and as expected the target areas are displayed in this component as bright pixels (Fig. 6b). Thus, the MNF4 was considered for enhancing carbonatite over the Gleibat Lafhouda area.

4.2. Mapping of iron oxide-apatite ores

The Fe-oxide/hydroxide minerals often exhibit differences in the spectral absorption between ASTER band 3 and band 4. As also shown in Figure 3, apatite exhibits absorption features similar to those of iron oxides with high reflectance in band 4 and minimum reflectance at band 3 to band 1 (Fig. 3). Consequently, the following band ratios; B4/B1, B4/B3, and B2/B1 were used to highlight the IOA ores. The band ratios B4/B1 and B4/B3 display curves nearer to the upper left corner with the highest AUC values (0.93 and 0.90 respectively; Fig. 7), in contrast, the band ratio B2/B1 shows low prediction accuracy (AUC = 0.58). Accordingly, the band B4/B1 (Fig. 8) was considered in this study as the most appropriate option for the IOA ore mapping. Additionally, the magnetite, hematite, goethite, limonite, and apatite were considered as the most indicative minerals for the IOA mineralization. These minerals show high reflectance in bands 4–6 and maximum absorption in VNIR bands 1–3 of the electromagnetic spectrum (Fig. 3). Thus, the bands 1, 3, 4, and 6 were selected as a spectral subset in PCA and MNF techniques for detecting the IOA ores.

The eigenvectors obtained from the PCA transformation on the spectral subset of ASTER bands 1, 3, 4, and 6 are shown in Table 5. The PC2 shows the loading of bands 1 and 3 positively (0.075 and 0.826 respectively) and bands 4 and 6 negatively (-0.246 and −0.502). This trend is the inverse of the spectral graphs for the indicative minerals in the IOA mineralization, where the apatite and most iron oxide/hydroxide minerals exhibit high reflectance in bands 4, 6, and maximum absorption in bands 3 and 1. This, gives the target areas dark pixels as shown in Figure 9a. Hence, the component (PC 2) was considered in this study to highlight the IOA ore.

The MNF transformation was performed on the same spectral subsets (bands 1, 3, 4, and 6) as the PCA. As shown in Table 6 there is a high loading difference between bands 1, 3 (-0.547, −0.776 respectively) and bands 4, 6 (0.288 and 0.123 respectively) in the first component (MNF 1). This is consistent with the spectral graphs of the indicative minerals of the IOA ore (e.g., apatite, hematite, goethite). Therefore, the target areas in this component appear as bright pixels (Fig. 9b). Consequently, it was chosen to enhance the capacity of delineating the IOA ore in the Gleibat Lafhouda area.

4.3. Methods integration and accuracy assessment

The above-selected components from the PCA and MNF transformations and the most appropriate band ratios were thresholded to separate the most anomalous pixels in each method. As shown in Figures 5, 6, 8, 9, the applied methods give different anomalous areas which might due to the difference in sensitivity of each technique to the materials present in the scene. To further enhance the correct occurrences of the desired material, an integrated map was generated by combining all the methods (i.e., band rationing, PCA, and MNF).

To perform the reclassification of the band ratio results, MNF and PCA components, the anomalous pixels that showed the possible carbonatite outcrops in B13/B14 and B6+B9/B7 band ratios were classified as 1 while the other pixels were given 0. Similarly, the anomalous pixels obtained as carbonatite from the selected component PC4 and MNF4 (Fig. 6) were classified as 1 and the other pixels were given 0 (see supplementary material Figure S1). After reclassification, we found that the resulted anomalous pixels from the TIR band ratio (BR(TIR)= B13/B14) show the most restricted areas of possible carbonatite outcrops and gives 1.89% of the total investigated area (Table 7). While, the SWIR band ratio (BR(SWIR) = (B6+B9)/B7) with the PCA and MNF components give a large number of anomalous pixels (6.15%, 6.45%, and 2.17% of the total area, respectively). Thus, the TIR band ratio was resampled to 15 m and multiplied by the other components as the following formula: [BR(TIR)*(BR(SWIR)+PCA+MNF)]. As a result, three classes have been created depending on the number of the involved methods in each class (Table 7; Fig. 10). In details, the class 1 represents areas where only one of the three methods — i.e., BR (SWIR), PCA, or MNF gives carbonatite occurrences with the BR(TIR), the class 2 represents those areas where two methods have common anomalous pixels with the BR(TIR), and the class 3 displays the area where the four methods give simultaneously the possible carbonatite outcrops. The three classes show a decrease in the number of anomalous carbonatite pixels from class 1 to class 3. Classes 1 and 2 represent 0.52% and 0.20% of the total area, respectively, whereas class 3 has only 0.16%.

The band ratio (BR= B4/B1) used to highlight the IOA mineralization and the resulted components from PCA and MNF (Figs. 8, 9) were thresholded to separate the most anomalous pixels (see supplementary material Figures S2, S3). The band ratio (B4/B1) shows a much-restricted area of the anticipated IOA ore, only 0.084% of the total area. However, the other components (PCA and MNF) show a slightly higher number of anomalous pixels for PCA (0.679%) and a higher number for MNF transformation (5.736%; Table 8). Therefore, the band ratio (BR= B4/B1) was multiplied by the other components to generate an integrated map of the different methods. As shown in Figure 11 two classes are distinguished representing the variation in the number of methods involved in delineating anomalous areas. Class 1 represents areas where only one of the components (PCA or MNF) has common anomalous pixels with the band ratio (B4/B1), the class 2 highlights those areas where all the methods map simultaneously the possible IOA outcrops. The two classes have a close number of pixels with much reduced IOA anomalous surface areas in class 2 (0.036%; Table 8; Fig.11).

4.4. Field validation and geochemical portable XRF data

A field mission was carried out in the Gleibat Lafhouda area to validate the accuracy of the mapped occurrences of carbonatites and IOA ore (Figs. 10, 11). Most of the anomalies were visited and verified using the handheld XRF analyzer, and several samples were collected for petrographic characterization (see supplementary material Table S4). The outcropped carbonatites from Gleibat Lafhouda complex occur as fine- to medium-grained grey and white-brown rocks (Fig. 12 a–c). The carbonatites are associated with apatite-rich iron oxide mineralization, which is observed as massive to brecciated rocks of brown to dark brown color overlying the carbonatite intrusions (Fig. 12a, d).

The carbonatites are formed mainly by dolomite (0.1–1 mm in size; 70–90 vol.% of the rock), apatite (0.2–2 mm; 0.5–10 vol.%), and iron oxides (magnetite and hematite) with subordinate calcite, quartz, clinohumite and phlogopite (Fig. 13a–c). The carbonatites are frequently crosscut by tiny veins of iron oxides and calcite (Fig. 13d). The IOA mineralization consists mainly of Fe-oxide/hydroxide minerals (hematite, goethite, magnetite, and limonite) and apatite (5 − 40 vol.%), quartz, and subordinate calcite as interstitial filling, and monazite and columbite as accessory minerals. The apatite occurs as euhedral crystals up to 8 cm in size (Figs. 12d, 13e), and often associated with numerous fine monazite grains which occur as inclusions and/or nearby its rims (Fig. 13f).

The carbonatites are primarily composed of CaO (14.9 − 57.7 wt.%) and MgO (2.2 − 30.3 wt.%) reflecting their magnesiocarbonatite affinity. Their P_2O_5 content ranges from 0.1 wt.% to 7.2 wt.% with about 1.5 wt.% in average. They are characterized by low silica content (~ 2.7 wt.% SiO_2 in average) , moderate Fe_2O_3 content (~ 6.3 wt.% in average), and very low TiO_2 and MnO concentrations (0 − 2.4 wt.% and 0.3 − 1.7 wt.%). The IOA ore is characterized by high Fe_2O_3 and SiO_2 concentrations (~ 2 − 54 wt.% and ~ 4 − 86 wt.%, respectively) with variable CaO and P_2O_5 contents (~ 0.3 − 44.6 wt.% and 0.2 − 33.9 wt.%, respectively) and low TiO_2 and MnO contents (0 − 1.9 wt.% and 0.1 − 1.6 wt.%, respectively).

4.5. Supervised classification-based facies mapping

The result obtained from the superimposition of the different methods were used to perform a supervised classification. As confirmed by field observations, the class 3 (Fig. 10) was of high accuracy and the carbonatites were found exposed at outcrop level. Similarly, for iron oxide-apatite ore, class 2 (Fig. 11) was the one that coincides well with the IOA ore outcrops. Therefore, these two classes were considered for performing the lithological classification in the Gleibat Lafhouda carbonatite complex. The results show an overall accuracy of 98.02% with a kappa coefficient of 0.86%. As shown in Figure 14, most of the mapped zones as carbonatites match the three intrusions of the Gleibat Lafhouda complex, with few outcrops scattered in the surrounding plain. The major proportion of mapped IOA ore zones occurs predominantly in the Al Fernan and Lafhouda intrusions (Fig. 14a, b) with only a minor proportion in the Drag intrusion (Fig 14c), which might due to their low exposed outcrops caused by the widespread sand cover.

5. Discussion

In this study, an integrated approach based on remotely sensed ASTER data, field observations, and portable XRF analyses has been performed for mapping carbonatite and associated iron oxide-apatite deposits in the large Gleibat Lafhouda area in the southern Moroccan province. Several band ratios have been applied to better distinguish the carbonatite outcrops from the country rocks of the studied area. The carbonate index in the TIR region (B13/B14) has given better results for carbonatite mapping compared to other carbonate indices in the SWIR region (Fig. 4). However, this index might give some false carbonatite anomalies when applied separately, and this is likely due to the similarity of the carbonate spectral characteristics with other sedimentary rocks in the area. In fact, as shown in Figure 5a, some anomalous bright pixels were observed in the right down corner of the scene with compared index values as those that fit with the carbonatite intrusions. These false anomalies were likely related to the presence of clay and other sulfate minerals of Sebkha zone (Fig. 1). Although, the band ratio (B6+B9)/B7 has more sensitivity to magnesiocarbonatites compared to (B6/B8)*(B9/B8) and (B6+B8)/B7 previously proposed for carbonate minerals in the SWIR region (Fig.4; Ninomiya 2002; Rowan and Mars 2003; Ninomiya et al. 2005; Mars and Rowan 2011). This band ratio presents false anomalies which likely due to the presence of mafic minerals-rich lithologies, such as amphiboles which have high sensitivities in the SWIR region (Rowan et al. 2005). Nevertheless, when combining these band ratios with resulted anomalies from PCA and

MNF, the areas with common anomalies from this combination showed better agreement with carbonatite outcrops in the field. This demonstrates the importance of combining the above methods. As shown in Figure 10, most of the points sampled as carbonatites fit with the common anomalous pixels, with few points that were only detected by two or three methods (class 1 or class 2; Fig 10). This is probably due to the small outcrop surfaces at some point and the large extension of sand cover, as well as the different sensitivity of the applied methods.

The bands 1, 2, 5, and 8 appear as the most suitable spectral subsets for performing the transformation techniques (i.e., PCA, MNF) where the most indicative minerals for carbonatite rocks have diagnostic absorption in these bands. Indeed, the carbonates have significant narrow absorption in band 8 due to C–O bonds (Mars and Rowan 2010) and high reflectance in band 5. Additionally, the dominant presence of ferrous and ferric iron in the carbonatite especially the ankeritic and the dolomitic carbonatites as those of the Gleibat Lafhouda makes the combination of Fe^{2+} and Fe^{3+} (bands 1, 2) and CO_3 (band 8) more suitable for carbonatite mapping. Furthermore, the intense Fe^{2+} absorption in carbonatites can either be used to distinguish them from most of the sedimentary carbonates which rarely exhibit this character (e.g., Rowan et al. 1986).

Several band ratios have been applied in this study to distinguish the most successful one for enhancing the mapping of the iron oxide-apatite deposits. The band ratios (B4/B3) and (B2/B1) in the VNIR region have been widely used to highlight iron-rich formations (Soe et al. 2005; Gopinathan et al. 2020). The band ratio B4/B3 gives relatively elevated detection rates compared to B2/B1 for apatite-rich iron oxide mineralization. However, it presents limits of application especially when mafic rocks such as gabbro are present in the analyzed scene, where these rocks have index values identical to those of the IOA ore. Instead, the band ratio (B4/B1) applied here shows a high ability to anticipate correct occurrences of the apatite-rich iron oxide mineralization and can be the best option to enhance the IOA deposits. As confirmed by our field observations, this band ratio when combined with iron anomalies obtained from PCA and MNF transformations gives high precision limits of the IOA ore outcrops (Fig. 11).

Our results were validated through field surveys and in-situ handheld XRF geochemical analysis, and show good agreement with previous geological maps of the area (Rjimati et al. 2002; ONHYM 2016a; ONHYM 2016b). The field data were used to validate several anomalous zones given by the different methods and validate the performed classification. The classified zones by the ML-algorithm as carbonatite and IOA ore are concordant with the common anomalies detected by method combinations (Figs. 10, 11). Indeed, the classified carbonatite pixels (Fig. 14) show more surface extension and complete those observed in class 3 of the integrated map (Fig. 10). Similarly, the classified pixels as IOA ores (Fig. 14) fit with class 2 of the integrated map (Fig. 11) and display the IOA outcrops extension. The ML algorithm based-classification has an overall accuracy of 98% which shows the good distribution of the mapped facies. The kappa coefficient calculated using the confusion matrix method is 0.86, which is considered as an excellent agreement category of the Kappa coefficient (e.g., Monserud and Leemans 1992). Furthermore, most of the areas mapped as IOA ore (Fig. 14) are surrounded by carbonatite, which is consistent with the field observations showing that they are predominantly overlying the carbonatite bodies (Fig. 12a). Additionally, the mapped zones as carbonatites match those of the three main intrusions where carbonatites are well exposed as observed in the previous maps from thr literature (Fig. 1). Several scattered bodies were highlighted for the first time in the surrounding plain, especially in the south of the area (Figs. 12c, 14). This might indicate the hidden extension of this carbonatite complex beneath the sand cover. However, further exploration work using core drilling and/or geophysical studies still necessary to better evaluate the lateral extension of this complex.

6. Conclusions

In this study, we demonstrate the significant information that can be retrieved from satellite remote sensing ASTER data for mineral exploration and geological mapping. The ASTER processed data coupled with field observations, portable XRF analyses, and petrographic characterization were examined to show their ability for identifying and mapping of carbonatite outcrops and related iron oxide-apatite mineralization. The combination of band ratios from TIR region (B13/14) and SWIR bands (B6+B9/B7) alongside with PCA, and MNF has proven to be reliable and probative to increase the accuracy of carbonatite mapping. Based on spectral properties of most indicative minerals of carbonatites (e.g., carbonates, apatite, phlogopite, iron oxides) a spectral subset (bands: 1, 2, 5, and 8) was determined to perform the PCA and MNF transformations. The appropriate component from each transformation method was selected by analyzing the eigenvalue loadings. This approach has also proven to be applicable for discriminating the iron oxide-apatite mineralization from carbonatite rocks over a large area. Although the band ratio B4/B1 has given a high ability to predict IOA anomalous areas, its integration with results of PCA and MNF has improved the accuracy to delineate the correct IOA ore occurrences. The mapped zones simultaneously using combined methods were consistent with the field observations. Thus, they were subjected to ML algorithm-based classification to delimit the extension of the mapped facies.

The developped approach has been applied successfully in the Archean terrains of the Oulad Dlim massif, and may represent a useful tool for highlighting other potential areas, especially under the same geographic and atmospheric conditions. Overall, the obtained results have several implications for the use of multispectral satellite imagery in general and ASTER data in particular, for carbonatite and IOA deposit exploration programs. Indeed, through this study, we highlight the benefit of the remote sensing-based approach as a powerful time- and cost-effective tool especially in zones where the conventional geological mapping is difficult and requires large investments. Further work for extending this approach on other alkaline complexes and related mineral deposits types may be of great interest especially, in arid regions.

Acknowledgment

This work was initiated in the frame of FP7-PEOPLE-IRSES project “MEDYNA” 2014–2017 (“Maghreb-EU research staff exchange on geoDYnamics, geohazards, and applied geology in North-west Africa”, Work Package #3: “Deep structures and mantle processes”), and was supported and funded by the UM6P project. The authors would like to thank the Military services and local authorities for their assistance during the entire period of field missions. The authors wish also to thank Bassou Zayi (UM6P-Geology & Sustainable Mining & UM6P–OCP Geo-Analytical Lab) and Christophe Nevado and Doriane Delmas (Géosciences Montpellier) for their help in sample and thin section preparations. We thank two anonymous reviewers for their constructive and helpful comments.

References

Abdelkareem M, El-Baz F. 2018. Characterizing hydrothermal alteration zones in Hamama area in the central Eastern Desert of Egypt by remotely sensed data. Geocarto Int. 33(12):1307–1325. https://doi.org/10.1080/10106049.2017.1325410

Abrams M. 2000. The Advanced Spaceborne Thermal Emission and Reflection Radiometer (ASTER): Data products for the high spatial resolution imager on NASA’s Terra platform. Int J Remote Sens. 21(5):847–859.

Ahmad A, Quegan S. 2012. Analysis of maximum likelihood classification on multispectral data. Appl Math Sci. 6(129):6425–6436.

Baldridge AM, Hook SJ, Grove CI, Rivera G. 2009. The ASTER spectral library version 2.0. Remote Sens Environ. 113(4):711–715. https://doi.org/10.1016/j.rse.2008.11.007

Bea F, Montero P, Haissen F, Molina JF, Lodeiro FG, Mouttaqi A, Kuiper YD, Chaib M. 2020. The Archean to Late-Paleozoic architecture of the Oulad Dlim Massif, the main Gondwanan indenter during the collision with Laurentia. Earth-Sci Rev. 208:103273. https://doi.org/10.1016/j.earscirev.2020.103273

Bea F, Montero P, Haissen F, Molina JF, Michard A, Lazaro C, Mouttaqi A, Errami A, Sadki O. 2016. First evidence for Cambrian rift-related magmatism in the West African Craton margin: The Derraman Peralkaline Felsic Complex. Gondwana Res. 36:423–438. https://doi.org/10.1016/j.gr.2015.07.017

Beirami RM, Tangestani MH. 2020. A New Band Ratio Approach for Discriminating Calcite and Dolomite by ASTER Imagery in Arid and Semiarid Regions. Nat Resour Res. 29(5):2949–2965. https://doi.org/10.1007/s11053-020-09648-w

Benaouda R, Kraemer D, Sitnikova M, Goldmann S, Freitag R, Bouali A, Mouttaqi A, El Haloui R, Essaadaoui M, Bau M. 2020. Thorium-poor monazite and columbite-(Fe) mineralization in the Gleibat Lafhouda carbonatite and its associated iron-oxide-apatite deposit of the Ouled Dlim Massif, South Morocco. Gondwana Res. 77:19–39. https://doi.org/10.1016/j.gr.2019.06.011

Bouabdellah M, Hoernle K, Kchit A, Duggen S, Hauff F, Klugel A, Lowry D, Beaudoin G. 2010. Petrogenesis of the Eocene Tamazert Continental Carbonatites (Central High Atlas, Morocco): Implications for a Common Source for the Tamazert and Canary and Cape Verde Island Carbonatites. J Petrol. 51(8):1655–1686. https://doi.org/10.1093/petrology/egq033

Bouabdli A, Dupuy C, Dostal J. 1988. Geochemistry of Mesozoic alkaline lamprophyres and related rocks from the Tamazert massif, High Atlas (Morocco). Lithos. 22(1):43–58. https://doi.org/10.1016/0024-4937(88)90028-X

Bronner G, Marchand J, Sougy J. 1985. Carte géologique du Maroc 1:1 000 000, feuille Sud, Ministère de l'Energie et des Mines, Direction de la Géologie. Rabat. [place unknown].

Chakhmouradian AR, Reguir EP, Kressall RD, Crozier J, Pisiak LK, Sidhu R, Yang P. 2015. Carbonatite-hosted niobium deposit at Aley, northern British Columbia (Canada): Mineralogy, geochemistry and petrogenesis. Ore Geol Rev. 64:642–666. https://doi.org/10.1016/j.oregeorev.2014.04.020

Clark RN. 1999. Spectroscopy of rocks and minerals, and principles of spectroscopy. In: Remote Sens Earth Sci Man Remote Sens. Vol. 3. 3rd ed.: John Wiley & Sons, New York; p. 3–58.

Cooley T, Anderson GP, Felde GW, Hoke ML, Ratkowski AJ, Chetwynd JH, Gardner JA, Adler-Golden SM, Matthew MW, Berk A, et al. 2002. FLAASH, a MODTRAN4-based atmospheric correction algorithm, its application and validation. In: IEEE Int Geosci Remote Sens Symp [Internet]. Vol. 3. Toronto, Ont., Canada: IEEE; [accessed 2021 Jan 7]; p. 1414–1418. https://doi.org/10.1109/IGARSS.2002.1026134

Crósta AP, De Souza Filho CR, Azevedo F, Brodie C. 2003. Targeting key alteration minerals in epithermal deposits in Patagonia, Argentina, using ASTER imagery and principal component analysis. Int J Remote Sens. 24(21):4233–4240. https://doi.org/10.1080/0143116031000152291

Duda K, Daucsavage J, Siemonsma D, Brooks B, Oleson R, Meyer D, Doescher C. 2015. Advanced spaceborne thermal emission and reflection radiometer (aster) level 1 precision terrain corrected registered at-sensor radiance product (ast_l1t). US Geol Surv USA.

Fakhari S, Jafarirad A, Afzal P, Lotfi M. 2019. Delineation of hydrothermal alteration zones for porphyry systems utilizing ASTER data in Jebal-Barez area, SE Iran. Iran J Earth Sci. 11(1):80–92.

Fujisada H. 1995. Design and performance of ASTER instrument. In: Adv -Gener Satell [Internet]. Vol. 2583. [place unknown]: International Society for Optics and Photonics; [accessed 2019 Apr 3]; p. 16–26. https://doi.org/10.1117/12.228565

Gärtner A, Villeneuve M, Linnemann U, Gerdes A, Youbi N, Hofmann M. 2016. Similar crustal evolution in the western units of the Adrar Souttouf Massif (Moroccan Sahara) and the Avalonian terranes: Insights from Hf isotope data. Tectonophysics. 681:305–317. https://doi.org/10.1016/j.tecto.2015.11.030

Gärtner A, Youbi N, Villeneuve M, Sagawe A, Hofmann M, Mahmoudi A, Boumehdi MA, Linnemann U. 2017. The zircon evidence of temporally changing sediment transport—the NW Gondwana margin during Cambrian to Devonian time (Aoucert and Smara areas, Moroccan Sahara). Int J Earth Sci. 106(8):2747–2769. https://doi.org/10.1007/s00531-017-1457-x

Gopinathan P, Parthiban S, Magendran T, Fadhil Al-Quraishi AM, Singh AK, Singh PK. 2020. Mapping of ferric (and ferrous (iron oxides distribution using band ratio techniques with ASTER data and geochemistry of Kanjamalai and Godumalai, Tamil Nadu, south India. Remote Sens Appl Soc Environ. 18:100306. https://doi.org/10.1016/j.rsase.2020.100306

Green AA, Berman M, Switzer P, Craig MD. 1988. A transformation for ordering multispectral data in terms of image quality with implications for noise removal. IEEE Trans Geosci Remote Sens. 26(1):65–74. https://doi.org/10.1109/36.3001

Guha A, K VK. 2016. New ASTER derived thermal indices to delineate mineralogy of different granitoids of an Archaean Craton and analysis of their potentials with reference to Ninomiya's indices for delineating quartz and mafic minerals of granitoids—An analysis in Dharwar Craton, India. Ore Geol Rev. 74:76–87. https://doi.org/10.1016/j.oregeorev.2015.10.033

Hunt GR. 1977. Spectral signatures of particulate minerals in the visible and near infrared. Geophysics.:501–513.

Khan A, Faisal S, Shafique M, Khan S, Bacha AS. 2020. ASTER-based remote sensing investigation of gypsum in the Kohat Plateau, north Pakistan. Carbonates Evaporites. 35(1):3. https://doi.org/10.1007/s13146-019-00543-x

Kogarko L. 2018. Chemical Composition and Petrogenetic Implications of Apatite in the Khibiny Apatite-Nepheline Deposits (Kola Peninsula). Minerals. 8(11):532. https://doi.org/10.3390/min8110532

Kokaly RF, Clark RN, Swayze GA, Livo KE, Hoefen TM, Pearson NC, Wise RA, Benzel WM, Lowers HA, Driscoll RL, Klein AJ. 2017. USGS Spectral Library Version 7 [Internet]. U.S. Geological Survey. https://doi.org/10.3133/ds1035

Loughlin WP. 1991. Principal Component Analysis for alteration mapping. Photogramm Eng Remote Sens. 57:1163–1169.

Mariano AN. 1989. Nature of economic mineralization in carbonatites and related rocks. In: Carbonatites Genes Evol. Unwin Hyman, London; p. 149–176.

Marks MAW, Schilling J, Coulson IM, Wenzel T, Markl G. 2008. The Alkaline-Peralkaline Tamazeght Complex, High Atlas Mountains, Morocco: Mineral Chemistry and Petrological Constraints for Derivation from a Compositionally Heterogeneous Mantle Source. J Petrol. 49(6):1097–1131. https://doi.org/10.1093/petrology/egn019

Mars JC, Rowan LC. 2010. Spectral assessment of new ASTER SWIR surface reflectance data products for spectroscopic mapping of rocks and minerals. Remote Sens Environ. 114(9):2011–2025. https://doi.org/10.1016/j.rse.2010.04.008

Mars JC, Rowan LC. 2011. ASTER spectral analysis and lithologic mapping of the Khanneshin carbonatite volcano, Afghanistan. Geosphere. 7(1):276–289. https://doi.org/10.1130/GES00630.1

Michard A, Saddiqi O, Chalouan A, de Lamotte DF. 2008. Continental evolution: The geology of Morocco: Structure, stratigraphy, and tectonics of the Africa-Atlantic-Mediterranean triple junction. (Vol. 116) : Springer.

Michard A, Soulaimani A, Hoepffner C, Ouanaimi H, Baidder L, Rjimati EC, Saddiqi O. 2010. The South-Western Branch of the Variscan Belt: Evidence from Morocco. Tectonophysics. 492(1–4):1–24. https://doi.org/10.1016/j.tecto.2010.05.021

Monserud RA, Leemans R. 1992. Comparing global vegetation maps with the Kappa statistic. Ecol Model. 62(4):275–293. https://doi.org/10.1016/0304-3800(92)90003-W

Montero P, Haissen F, El Archi A, Rjimati E, Bea F. 2014. Timing of Archean crust formation and cratonization in the Awsard-Tichla zone of the NW Reguibat Rise, West African Craton: A SHRIMP, Nd–Sr isotopes, and geochemical reconnaissance study. Precambrian Res. 242:112–137. https://doi.org/10.1016/j.precamres.2013.12.013

Montero P, Haissen F, Mouttaqi A, Molina JF, Errami A, Sadki O, Cambeses A, Bea F. 2016. Contrasting SHRIMP U–Pb zircon ages of two carbonatite complexes from the peri-cratonic terranes of the Reguibat Shield: Implications for the lateral extension of the West African Craton. Gondwana Res. 38:238–250. https://doi.org/10.1016/j.gr.2015.12.005

Ninomiya Y. 2002. Mapping quartz, carbonate minerals, and mafic-ultramafic rocks using remotely sensed multispectral thermal infrared ASTER data [Internet]. In: Maldague XP, Rozlosnik AE, editors. Vol. 4710. [accessed 2019 Apr 4]; p. 191–202. https://doi.org/10.1117/12.459566

Ninomiya Y, Fu B. 2016. Regional Lithological Mapping Using ASTER-TIR Data: Case Study for the Tibetan Plateau and the Surrounding Area. Geosciences. 6(3):39. https://doi.org/10.3390/geosciences6030039

Ninomiya Y, Fu B, Cudahy TJ. 2005. Detecting lithology with Advanced Spaceborne Thermal Emission and Reflection Radiometer (ASTER) multispectral thermal infrared "radiance-at-sensor" data. Remote Sens Environ. 99(1–2):127–139. https://doi.org/10.1016/j.rse.2005.06.009

Nykänen V, Lahti I, Niiranen T, Korhonen K. 2015. Receiver operating characteristics (ROC) as validation tool for prospectivity models — A magmatic Ni–Cu case study from the Central Lapland Greenstone Belt, Northern Finland. Ore Geol Rev. 71:853–860. https://doi.org/10.1016/j.oregeorev.2014.09.007

O'Brien H, Heilimo E, Heino P. 2015. The Archean Siilinjärvi Carbonatite Complex. In: Mineral Deposits of Finland. Elsevier; [accessed 2020 Oct 6]; p. 327–343. https://doi.org/10.1016/B978-0-12-410438-9.00013-3

Oliveira SMB de, Imbernon RAL. 1998. Weathering alteration and related REE concentration in the Catalão I carbonatite complex, central Brazil. J South Am Earth Sci. 11(4):379–388. https://doi.org/10.1016/S0895-9811(98)00024-8

ONHYM. 2016a. Nb, Ta, U, Fe and REE mineralization in the Glibat Lafhouda carbonatites (southern provinces, Morocco). Rabat: Office National des Hydrocarbures et des Mines.

ONHYM. 2016b. Drag and Al Farnan carbonatites (Nb, Ta, REE, U, Fe) (southern provinces, Morocco). Rabat: Office National des Hydrocarbures et des Mines.

Ouabid M, Raji O, Dautria J-M, Bodinier J-L, Parat F, El Messbahi H, Garrido CJ, Ahechach Y. 2021. Petrological and geochemical constraints on the origin of apatite ores from Mesozoic alkaline intrusive complexes, Central High-Atlas, Morocco. Ore Geol Rev. 136:104250. https://doi.org/10.1016/j.oregeorev.2021.104250

Pour AB, Hashim M. 2011. Application of advanced spaceborne thermal emission and reflection radiometer (ASTER) data in geological mapping. Int J Phys Sci.:12.

Qalbi A, Mouttaqi A, Rjimati EC, Zemmouri A, Michard A, Saddiqi O. 2011. The Nb-Ta-U-REE Prospects of the Glibat Lafhouda Carbonatites (Awserd Province). In: New Geol Min Guideb Moroc. Rabat: Notes et Mémoires du Service geologique du Maroc, 564(9); p. 183–187.

Rajendran S, Nasir S. 2013a. ASTER spectral analysis of ultramafic lamprophyres (carbonatites and aillikites) within the Batain Nappe, northeastern margin of Oman: a proposal developed for spectral absorption. Int J Remote Sens. 34(8):2763–2795. https://doi.org/10.1080/01431161.2012.748941

Rajendran S, Nasir S. 2013b. ASTER mapping of limestone formations and study of caves, springs and depressions in parts of Sultanate of Oman. Environ Earth Sci. 71(1):133–146. https://doi.org/10.1007/s12665-013-2419-7

Rajendran S, Nasir S. 2014. ASTER spectral sensitivity of carbonate rocks – Study in Sultanate of Oman. Adv Space Res. 53(4):656–673. https://doi.org/10.1016/j.asr.2013.11.047

Raji O, Ouabid M, Bodinier J-L, El Messbahi H, Malainine C. 2021. An integrated approach for rapid delineation of K-rich syenites suitable as unconventional potash resources. Nat Resour Res. https://doi.org/In press

Rjimati EC, Michard A, Saddiqi O. 2011. Anti-Atlas occidental et Provinces sahariennes. In: Nouv Guid Géologiques Min Maroc. Vol. 6. Notes et Mémoires du Service Géologique du Maroc; p. 5–95.

Rjimati EC, Zemmouri A. 2002. Mémoire explicatif de la carte géologique du Maroc, feuille d'Awsard. Rabat, Notes et Mémoires du Service Géologique du Maroc.

Rjimati EC, Zemmouri A, Benlakhdim A, Amzaghro M. 2002. Carte Géologique du Maroc, 1: 50000, sheet Sabkhat Lahmayda. Notes et Mémoires du Service Géologique du Maroc.

Rowan LC, Kingston MJ, Crowley JK. 1986. Spectral reflectance of carbonatites and related alkalic igneous rocks; selected samples from four North American localities. Econ Geol. 81(4):857–871. https://doi.org/10.2113/gsecongeo.81.4.857

Rowan LC, Mars JC. 2003. Lithologic mapping in the Mountain Pass, California area using Advanced Spaceborne Thermal Emission and Reflection Radiometer (ASTER) data. Remote Sens Environ. 84(3):350–366. https://doi.org/10.1016/S0034-4257(02)00127-X

Rowan LC, Mars JC, Simpson CJ. 2005. Lithologic mapping of the Mordor, NT, Australia ultramafic complex by using the Advanced Spaceborne Thermal Emission and Reflection Radiometer (ASTER). Remote Sens Environ. 99(1–2):105–126. https://doi.org/10.1016/j.rse.2004.11.021

Sabins FF. 1999. Remote sensing for mineral exploration. Ore Geol Rev. 14(3–4):157–183. https://doi.org/10.1016/S0169-1368(99)00007-4

Shi X, Al-Arifi N, Abdelkareem M, Abdalla F. 2020. Application of remote sensing and GIS techniques for exploring potential areas of hydrothermal mineralization in the central Eastern Desert of Egypt. J Taibah Univ Sci. 14(1):1421–1432. https://doi.org/10.1080/16583655.2020.1825184

Soe M, Kyaw TA, Takashima I. 2005. Application of remote sensing techniques on iron oxide detection from ASTER and Landsat images of Tanintharyi coastal area, Myanmar.

Sougy J. 1962. Contribution à l'étude géologique des guelb Bou Leriah (region d'Aoucert, Sahara Espagnol). Bull Société Géologique Fr. S7-IV(3):436–445. https://doi.org/10.2113/gssgfbull.S7-IV.3.436

Tobin DC. 2007. Hyperspectral data noise characterization using principle component analysis: application to the atmospheric infrared sounder. J Appl Remote Sens. 1(1):013515. https://doi.org/10.1117/1.2757707

Toledo MCMD, Lenharo SLR, Ferrari VC, Fontan F, Parseval PD, Leroy G. 2004. The compositional evolution of apatite in the weathering profile of the Catalão I alkaline-carbonatitic complex, Goias, Brazil. Can Mineral. 42(4):1139–1158. https://doi.org/10.2113/gscanmin.42.4.1139

Verplanck PL, Mariano AN, Mariano A. 2016. Rare Earth Element Ore Geology of Carbonatites. In: Rare Earth Crit Elem Ore Depos [Internet]. Littleton, CO, USA: Society of Economic Geologists; [accessed 2020 Mar 27]. https://doi.org/10.5382/Rev.18.01

Vielreicher NM, Groves DI, Vielreicher RM. 2000. The Phalaborwa (Palabora) deposit and its potential connection to iron-oxide copper-gold deposits of Olympic Dam Type. Hydrothermal Iron-Oxide Copp-Gold Relat Depos Glob Perspect Ed TM Porter PGC Publ Adel Aust. 1:321–329.

Villeneuve M, Bellon H, El Archi A, Sahabi M, Rehault J-P, Olivet J-L, Aghzer AM. 2006. Événements panafricains dans l'Adrar Souttouf (Sahara marocain). Comptes Rendus Geosci. 338(5):359–367. https://doi.org/10.1016/j.crte.2006.02.008

Villeneuve M, El Archi A, Nzamba J. 2010. Les chaînes de la marge occidentale du Craton Ouest-Africain, modèles géodynamiques. Comptes Rendus Geosci. 342(1):1–10. https://doi.org/10.1016/j.crte.2009.12.002

Wang Z-Y, Fan H-R, Zhou L, Yang K-F, She H-D. 2020. Carbonatite-Related REE Deposits: An Overview. Minerals. 10(11):965. https://doi.org/10.3390/min10110965

Willet GC, Duncan RK, Rankin RA. 1989. Geology and economic evaluation of the Mt. Weld carbonatite, Laverton, Western Australia. In : Kimberlite and Related Rocks. Geol Soc Aust Spec. Publ No 14.

Xiuping Jia, Richards JA. 1994. Efficient maximum likelihood classification for imaging spectrometer data sets. IEEE Trans Geosci Remote Sens. 32(2):274–281. https://doi.org/10.1109/36.295042

Yazdi Z, Jafari Rad A, Aghazadeh M, Afzal P. 2018. Alteration Mapping for Porphyry Copper Exploration Using ASTER and QuickBird Multispectral Images, Sonajeel Prospect, NW Iran. J Indian Soc Remote Sens. 46(10):1581–1593. https://doi.org/10.1007/s12524-018-0811-1

Young KE, Evans CA, Hodges KV, Bleacher JE, Graff TG. 2016. A review of the handheld X-ray fluorescence spectrometer as a tool for field geologic investigations on Earth and in planetary surface exploration. Appl Geochem. 72:77–87. https://doi.org/10.1016/j.apgeochem.2016.07.003

Zaitsev AN, Terry Williams C, Jeffries TE, Strekopytov S, Moutte J, Ivashchenkova OV, Spratt J, Petrov SV, Wall F, Seltmann R, Borozdin AP. 2014. Rare earth elements in phoscorites and carbonatites of the Devonian Kola Alkaline Province, Russia: Examples from Kovdor, Khibina, Vuoriyarvi and Turiy Mys complexes. Ore Geol Rev. 64:477–498. https://doi.org/10.1016/j.oregeorev.2014.06.004

Zamyad M, Afzal P, Pourkermani M, Nouri R, Jafari MR. 2019. Determination of Hydrothermal Alteration Zones Using Remote Sensing Methods in Tirka Area, Toroud, NE Iran. J Indian Soc Remote Sens. 47(11):1817–1830. https://doi.org/10.1007/s12524-019-01032-3

Table 1. Acquisition characteristics of used ASTER images.

Location	**ASTER Data Granule ID**	**Date**	**Scene Center**
Gleibat Lafhouda	AST_L1T_00302032004114331_20150503031013_72511	2004 − 02-03	Y = 219 318 X = − 150 192
	AST_L1T_00302032004114323_20150503031013_72512	2004 − 02-03	Y = 224 653 X= − 148 929

Table 2. Spectral bands characteristics of the ASTER satellite imagery used in this study (Abrams 2000; Fujisada 1995).

Subsystem	Band No.	Spectral Range (μm)	Spatial Resolution	Signal Quantization Levels
VNIR	1	0.52 − 0.60	15 m	8 bits
	2	0.63 − 0.69		
	3 N	0.78 − 0.86		
	3B	0.78 − 0.86		
SWIR	4	1.600 − 1.700	30 m	8 bits
	5	2 .145 − 2 .185		
	6	2.185 − 2.225		
	7	2.235 − 2.285		
	8	2.295 − 2.365		
	9	2.360 − 2.430		
TIR	10	8 .125 − 8 .475	90 m	12 bits
	11	8 .475 − 8 .825		
	12	8. 925 − 9 .275		
	13	10.25 − 10.95		
	14	10.95 − 11.65		

Table 3. Eigenvector statistics of PCA on selected spectral bands (1, 2, 5, and 8) of ASTER data for detecting carbonatites in the Gleibat Lafhouda complex.

	PC 1	PC 2	PC 3	PC 4
band 1	0.32487	-0.49148	0.38085	0.71265
band 2	0.50349	-0.63138	-0.22113	-0.54678
band 5	0.54412	0.45181	0.64797	-0.28273
band 8	0.58728	0.39456	-0.62144	0.3365

Table 4. Transformation vectors of MNF analysis on the selected spectral bands (1, 2, 5, and 8) of ASTER data for detecting carbonatites in the Gleibat Lafhouda complex.

	MNF 1	MNF 2	MNF 3	MNF 4
band 1	0.589015	0.002968	-0.702081	-0.400167
band 2	-0.808076	-0.000017	-0.516876	-0.282583
band 5	0.007089	0.38938	-0.450348	0.803443
band 8	-0.00491	0.921072	0.192635	-0.338369

Table 5. Eigenvector statistics of PCA on the selected spectral bands (1, 3, 4, and 6) of ASTER data for detecting iron oxide-apatite ores in the Gleibat Lafhouda complex.

	PC 1	PC 2	PC 3	PC 4
band 1	0.31035	0.07494	0.946	-0.05606
band 3	0.48411	0.8258	-0.21261	0.19617
band 4	0.61189	-0.24584	-0.22379	-0.71769
band 6	0.54306	-0.50199	-0.09893	0.66581

Table 6. Transformation vectors of MNF analysis on the selected spectral bands (1, 3, 4, and 6) of ASTER data for detecting iron oxide-apatite ores in the Gleibat Lafhouda complex.

	MNF 1	MNF 2	MNF 3	MNF 4
band 1	-0.546736	0.387327	0.236915	-0.703512
band 3	-0.776457	-0.405508	0.188976	0.443808
band 4	0.288079	-0.003478	0.952867	0.095091
band 6	0.123305	-0.827967	0.014274	-0.546867

Table 7. Number, surface, and percentage of anomalous pixels mapped as carbonatites by all used methods.

Method	Number of pixels	surface area (Km^2)	Percentage (%)
BR(TIR)	66336	14.93	1.89
BR(SWIR)	215312	48.45	6.15
PCA	225844	50.81	6.45
MNF	76144	17.13	2.17
BR(TIR)*(BR(SWIR)+PCA+MNF) class1	18385	4.14	0.52
BR(TIR)*(BR(SWIR)+PCA+MNF) class2	6940	1.56	0.20
BR(TIR)*(BR(SWIR)+PCA+MNF) class3	5489	1.24	0.16

Table 8. Number, surface and percentage of anomalous pixels mapped as iron apatite-apatite mineralization by all used methods.

Method	Number of pixels	surface area (Km^2)	Percentage (%)
BR	2944	0.66	0.084
PCA	23773	5.35	0.679
MNF	200955	45.21	5.736
BR*(PCA+MNF) class1	1379	0.31	0.039
BR*(PCA+MNF) class2	1249	0.28	0.036

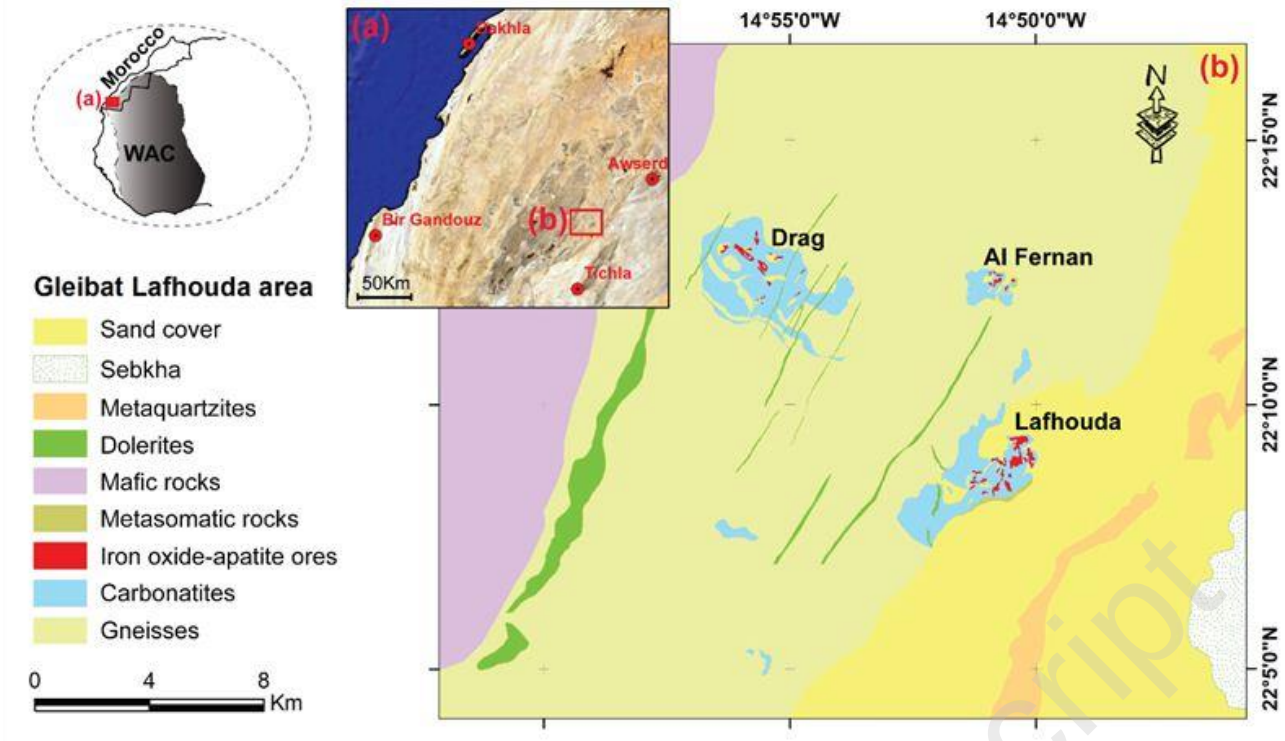

Figure 1. Map of the study area including (a) a Google Earth image showing the situation of the Gleibat Lafhouda complex in the Oulad Dlim massif at the NW margin of the West African Craton (WAC), and (b) simplified geological map of the Gleibat Lafhouda carbonatite complex. Data from Rjimati et al. (2002); ONHYM (2016a; 2016b).

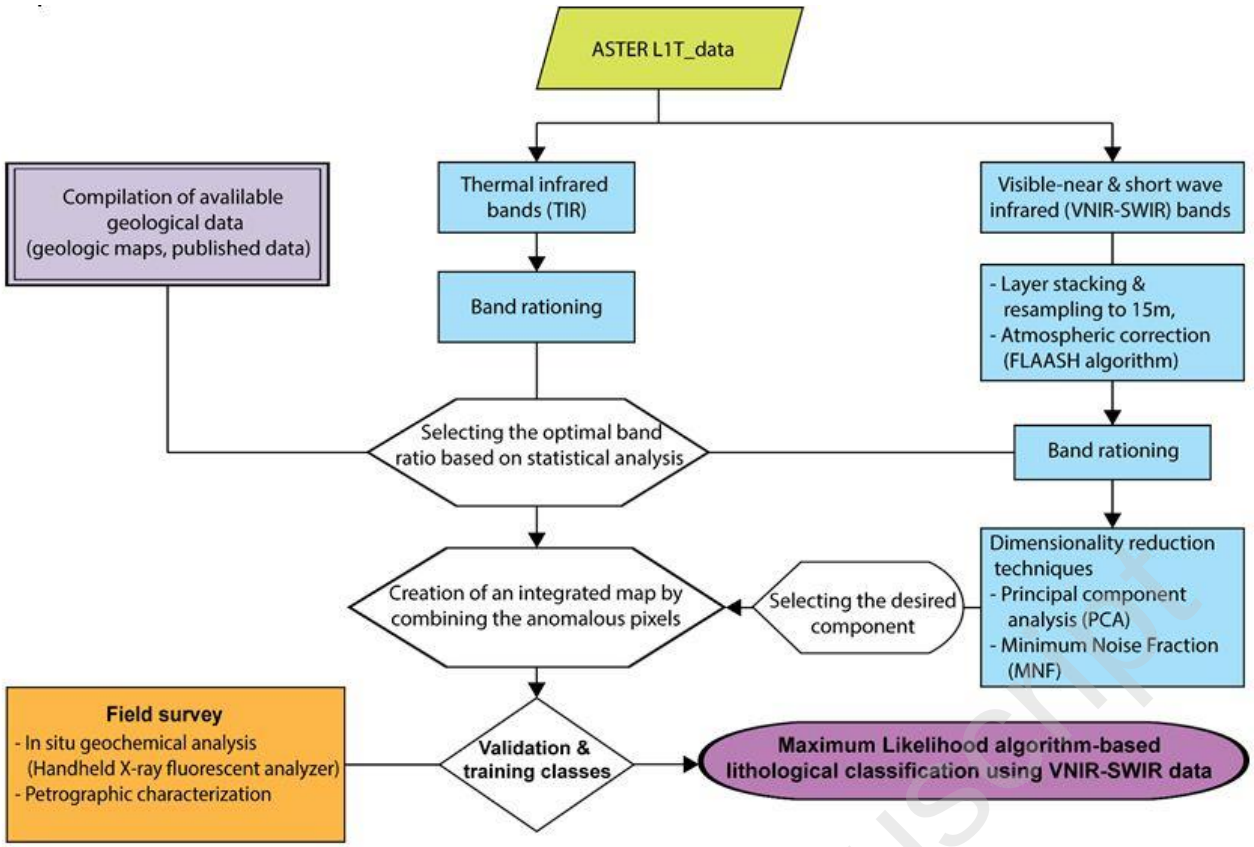

Figure 2. The workflow chart of the data sets and processing procedure used in this study.

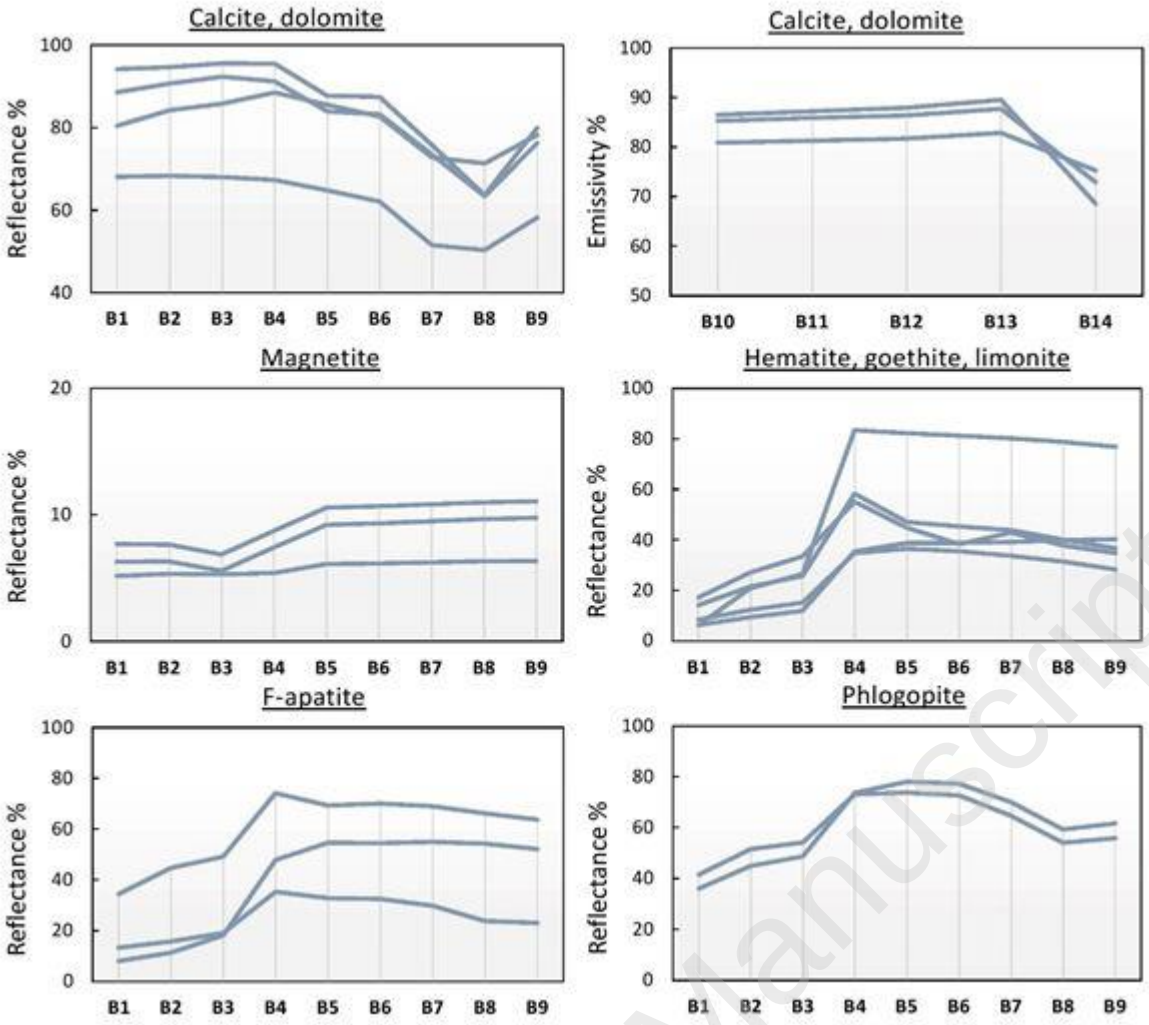

Figure 3. The spectral features of the carbonates, Fe-oxide/hydroxides, apatite, and phlogopite as the most carbonatite- and iron oxide-apatite-forming minerals. Data from the USGS spectral library, resampled according to ASTER bands (Kokaly et al. 2017).

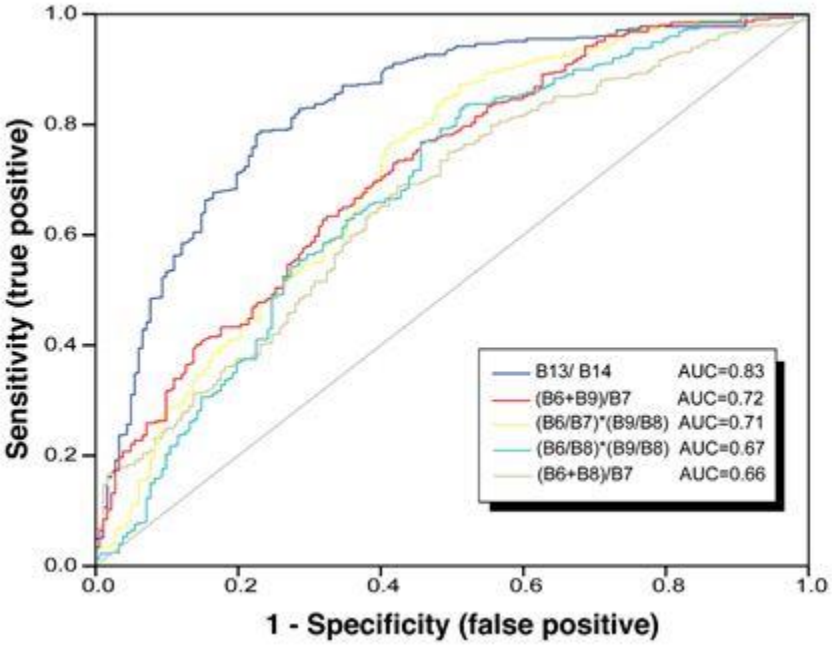

Figure 4. ROC curve and AUC values of carbonates predictive band ratios.

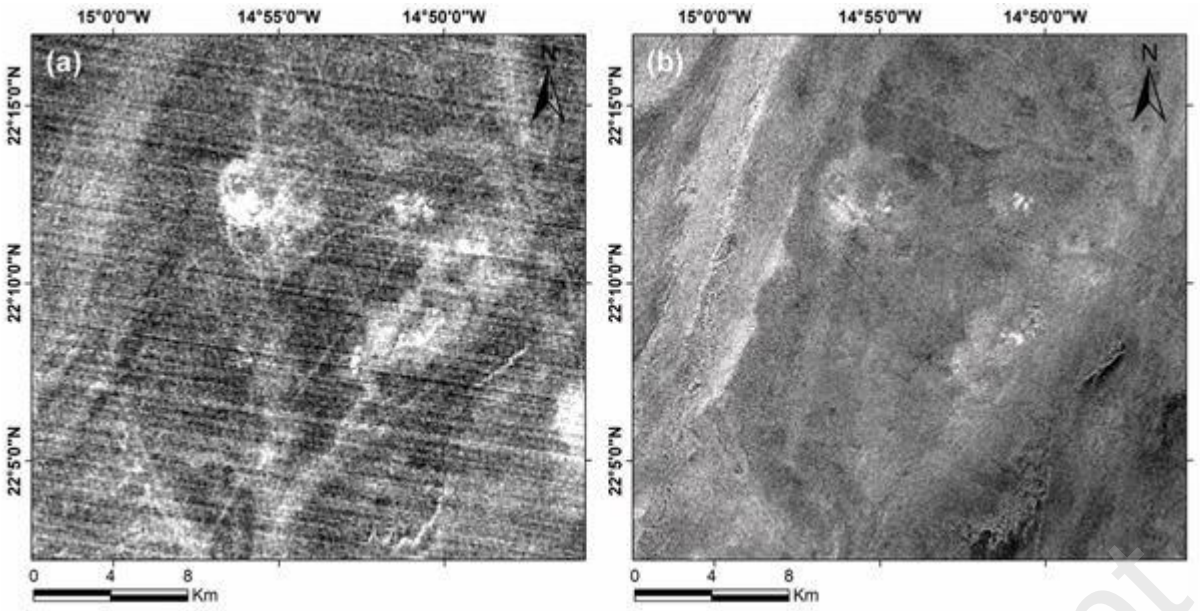

Figure 5. Grey scale images of **(a)** carbonate index in TIR ATSER bands (B13/B14) and **(b)** SWIR index (B6+B9)/B7 giving carbonatite anomalous zones in bright pixels.

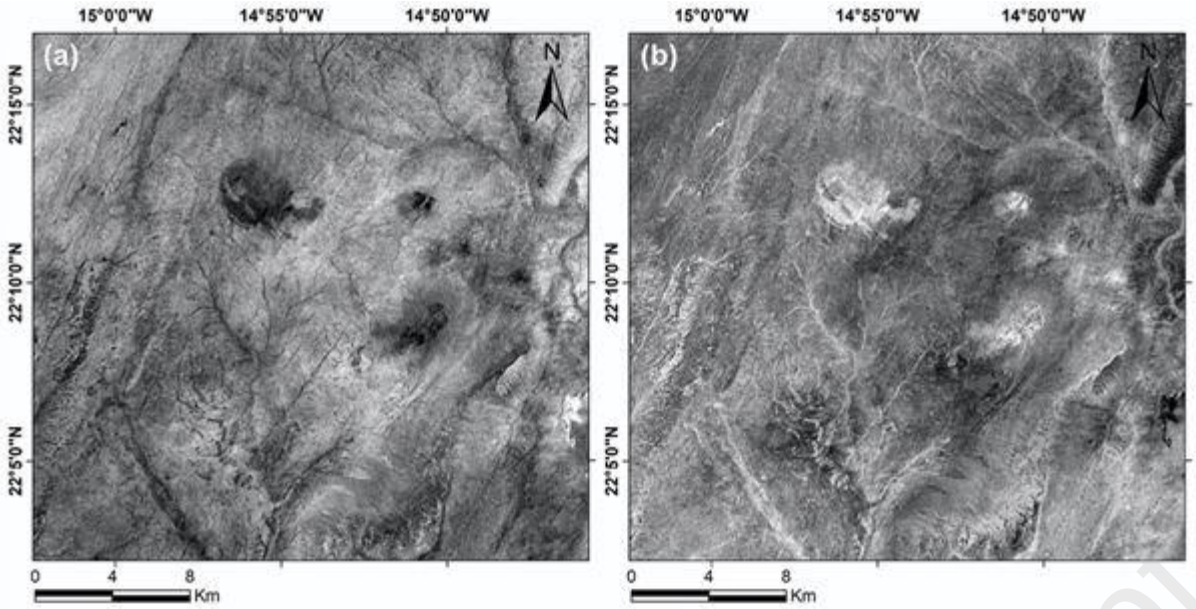

Figure 6. Greyscale images of selected components from the reduction transformation techniques applied on spectral bands 1, 2, 5, and 8 of ASTER data, highlighting carbonatites with dark pixels in PC4 **(a)**, and with bright pixels in MNF4 **(b)**.

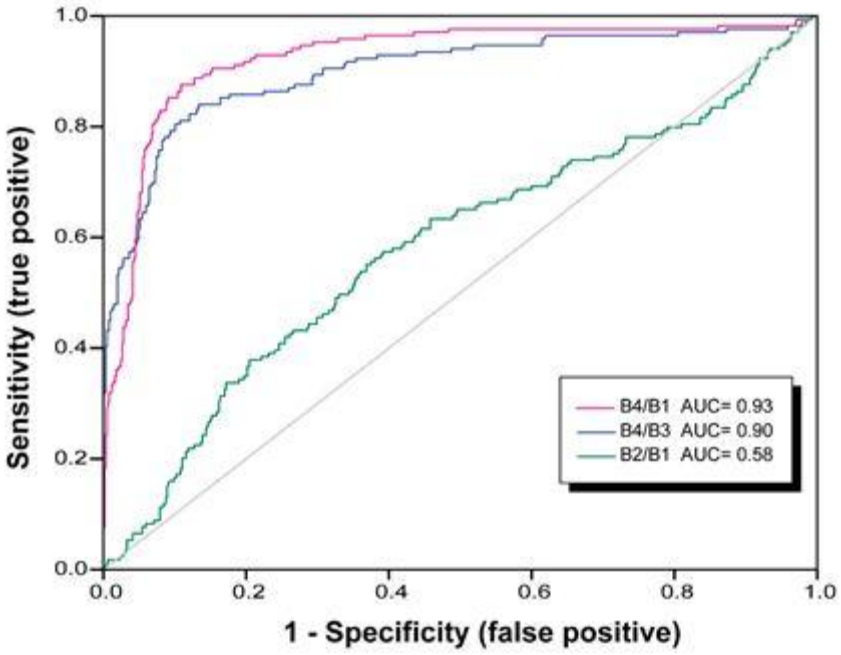

Figure 7. ROC curve and AUC values of iron oxide-apatite predictive band ratios.

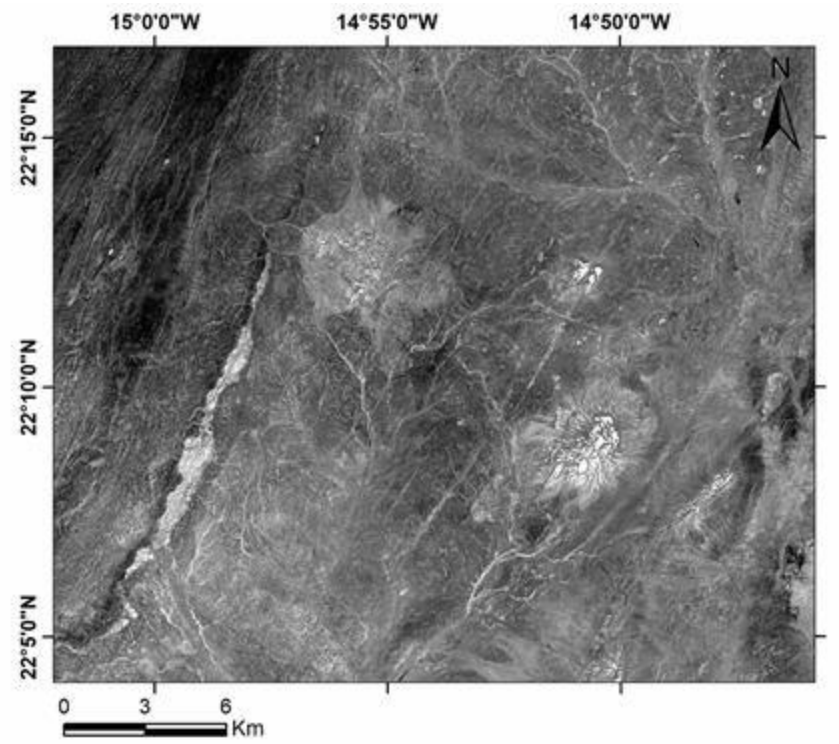

Figure 8. Iron oxide index (B4/B1) in the VNIR region on grayscale image showing in high bright pixels the anomalous areas of the iron oxide-apatite mineralization.

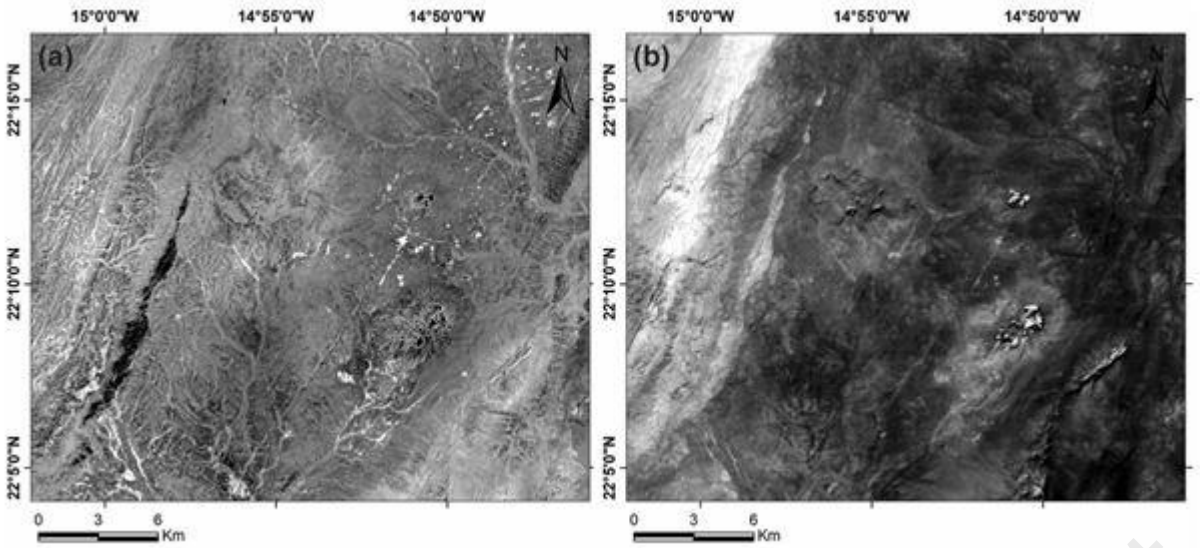

Figure 9. Greyscale images of selected components from the reduction transformation techniques applied on spectral bands 1, 3, 4, and 6 of ASTER data, (a) PC2 and (b) MNF1.

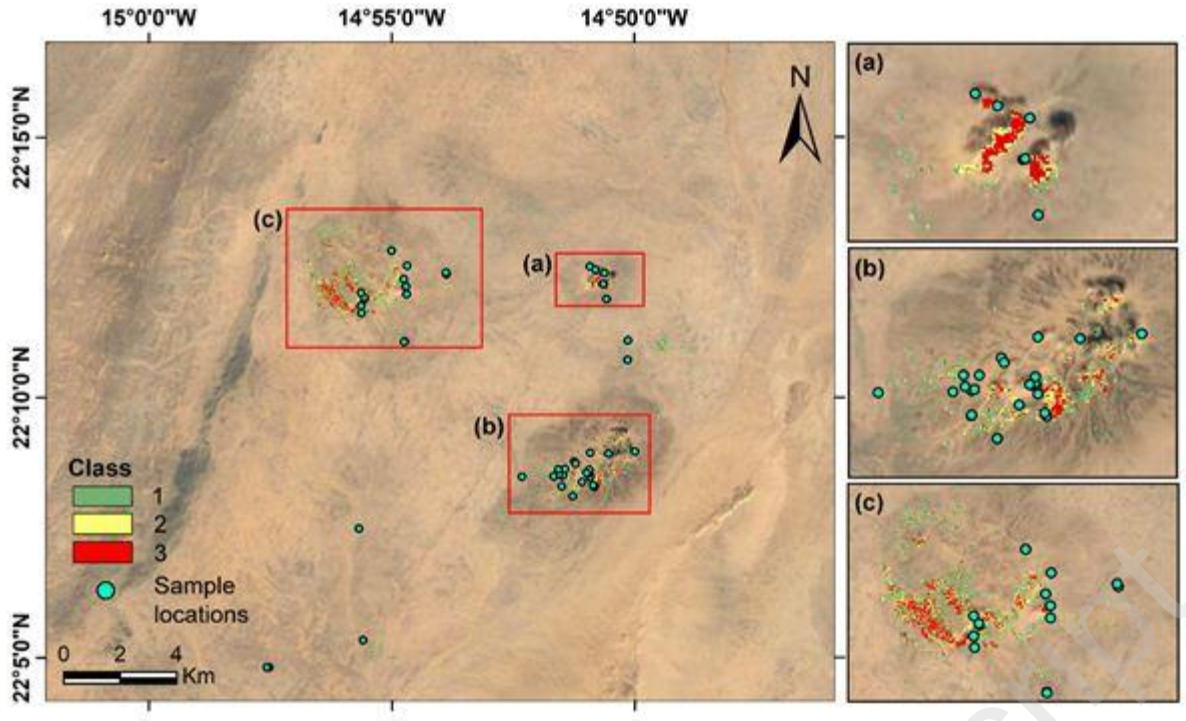

Figure 10. The designed integrated map showing anomalous carbonatite areas given by band ratio (B13/B14) with one method (green pixels) or two methods (yellow pixels), whereas the red pixels represent the areas given in common by all applied methods, which fit with the three magnesiocarbonatite intrusions of the Gleibat Lafhouda complex: Al Fernan **(a)**, Lafhouda **(b)** and Drag **(c).** The blue points correspond to carbonatite samples and the base map is a Google Earth image.

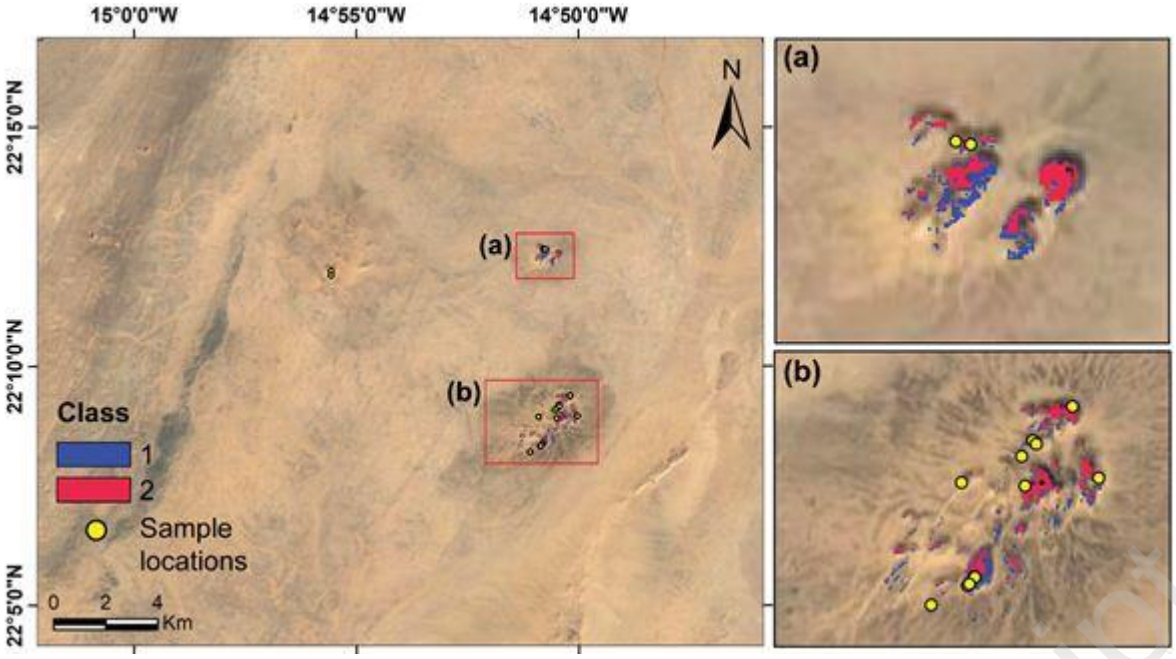

Figure 11. The integrated map of the IOA anomalous areas given by the band ratio (B4/B1) with PCA or MNF components (blue pixels) or both of them (red pixels), which were clearly observed in Al Fernan **(a)** and Lafhouda (**b)** intrusions of the Gleibat Lafhouda complex. The yellow points represent IOA ore samples and the base map is a Google Earth image.

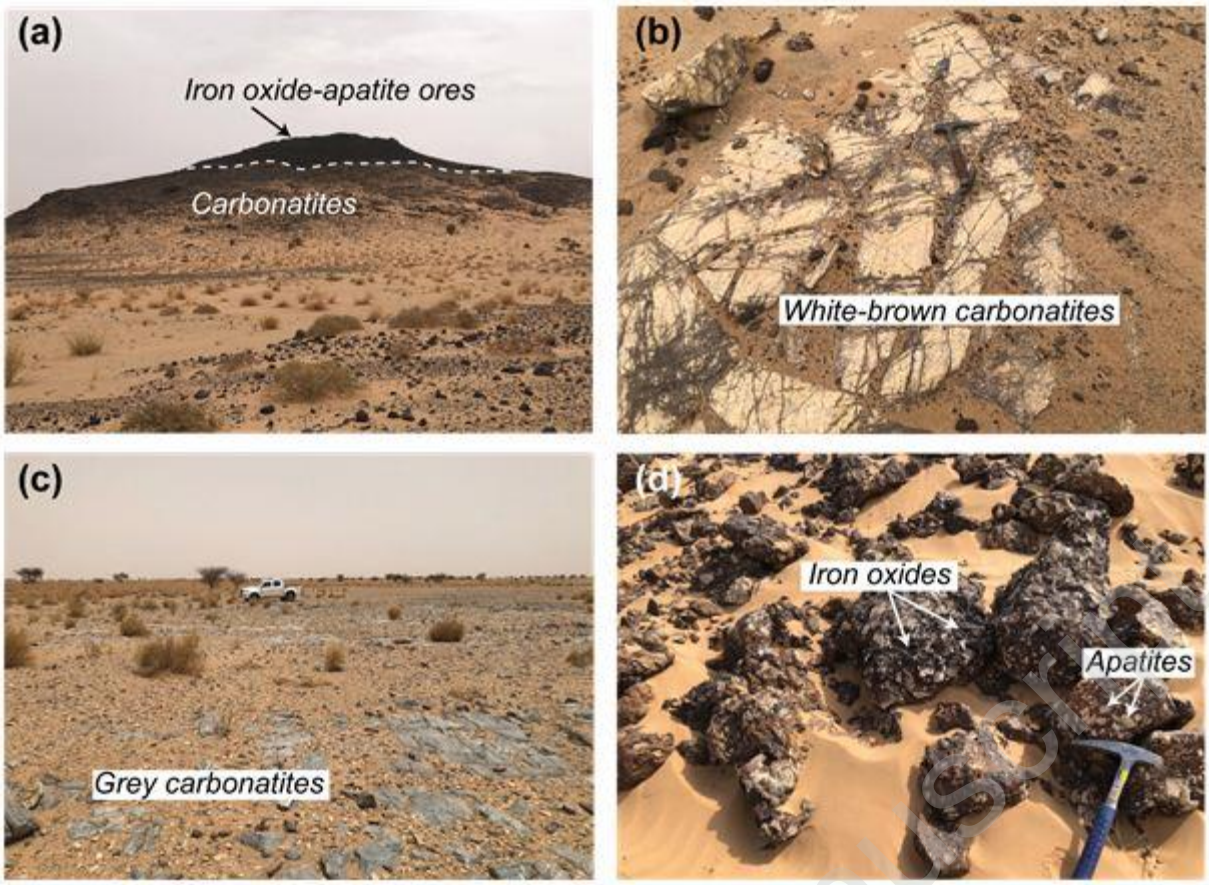

Figure 12. Field photographs of carbonatites and associated IOA ore in the Gleibat Lafhouda complex: **(a)** view towards the SW of the Lafhouda intrusion, **(b)** white-brown carbonatite crosscut by networks of tiny veins of iron oxides, **(c)** grey carbonatite facies, **(d)** the IOA ore with abundant euhedral apatite crystals.

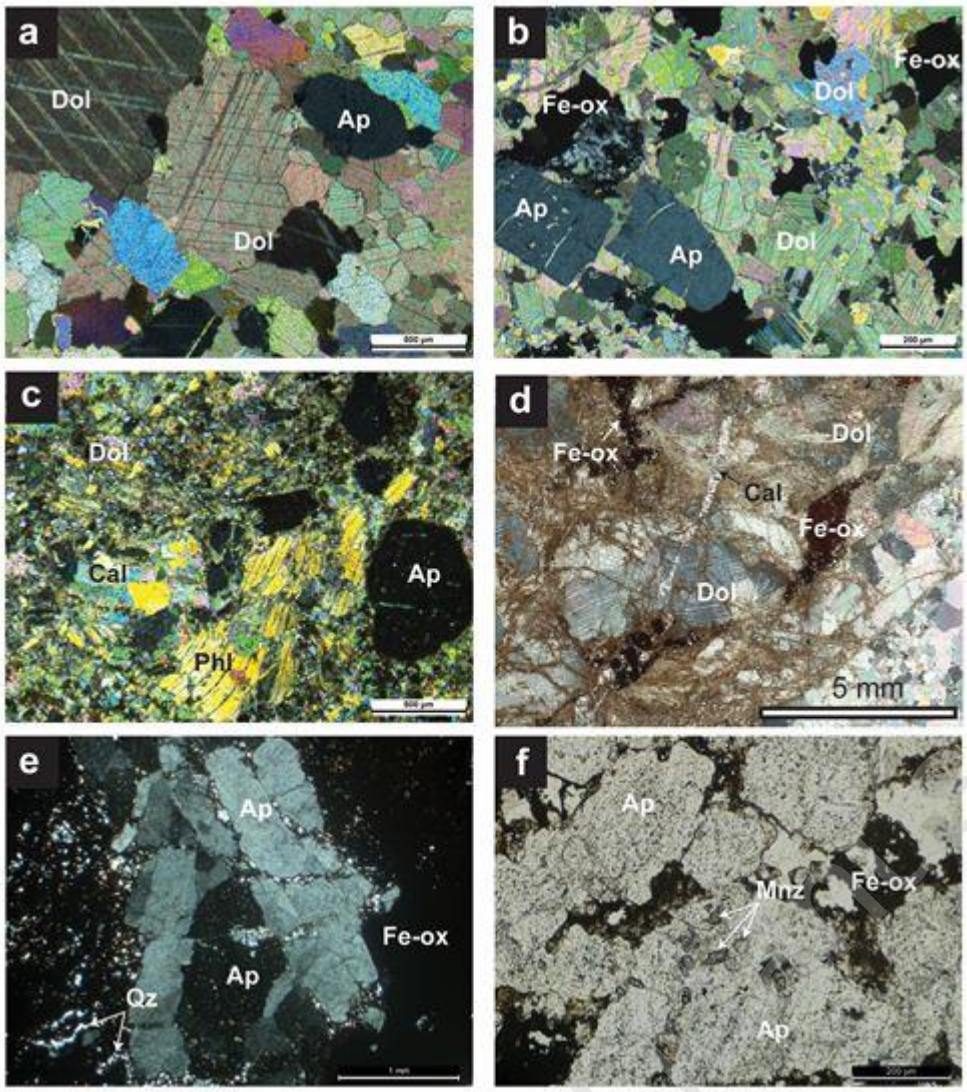

Figure 13. Microphotographs (microscope) showing the petrographic characteristics and the main rock-forming minerals of carbonatites and associated IOA ore: (**a**–**d**) carbonatites, (**e** and **f**) the iron oxide-apatite ore. apatite (Ap), calcite (Cal), dolomite (Dol), iron-oxides (Fe-ox), monazite (Mnz), phlogopite (Phl), quartz (Qz).

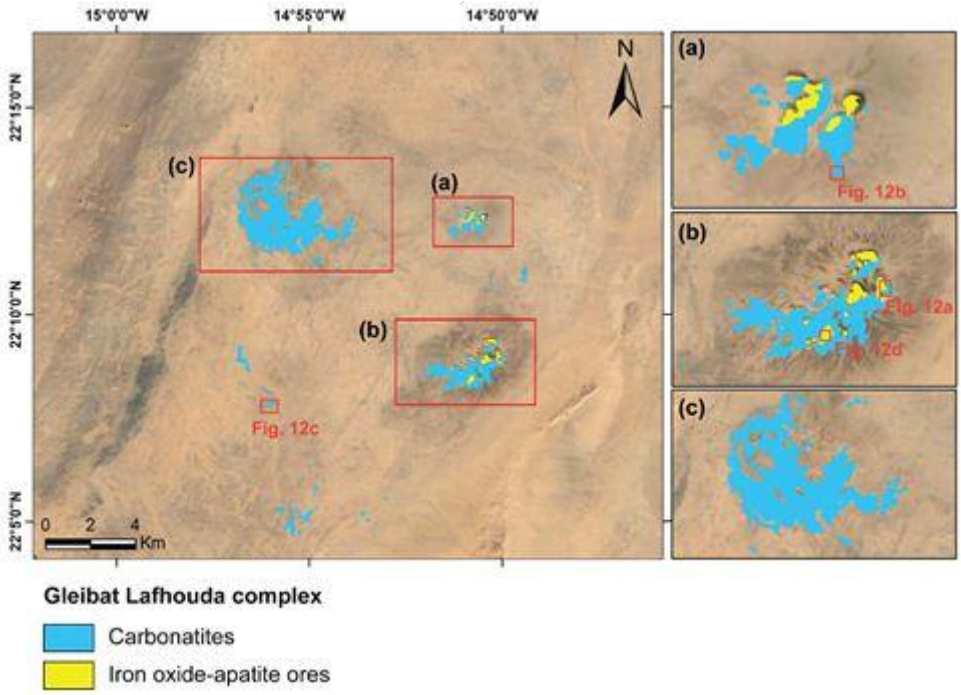

Figure 14. The ML algorithm-based classification using ASTER VNIR-SWIR data showing carbonatites and IOA ore outcrops in Al Fernan **(a)**, Lafhouda (**b)** and Drag **(c)** intrusions. The base map is a Google Earth image.